Supplementary Material for

Physical Realization of Non-Radiative Wireless Power Transmission Using Zenneck Waves

Sai Kiran Oruganti,[1] Jagannath Malik,[1] Jongwon Lee,[1] Woojin Park,[1]
Bonyoung Lee,[1] Seoktae Seo,[1] Dipra Paul,[1] Haksun Kim,[1]
Thomas Thundat,[2] and Franklin Bien.[1*]

January 3, 2019

1 Electrical Length: Half Wave Helical Transformer

Throughout 2015-18, authors conducted the experiments to study the voltage oscillation across the GBI resonator system. One such experiment carrying out power transfer across 80 mm metal wall can be seen in fig. S 1. This experiment uses the ground plate and wire arrangement to sustain a meaningful voltage oscillation across the terminals of the load (40 watts halogen).

Based on the experimental findings shown in fig. S 1, the authors tried to replace the equivalent RLC lumped elements(unsuccessfully so). The reasons behind the failure of RLC lumped elements based counterpoise were carefully and qualitatively investigated, through a series of experiments. It was observed that the planar structure of the receiver was unable to sustain a significant value of voltage and current. As shown in Fig. S 2 , the gap between the mesh and ground layer is g=1.5 mm. At a target frequency of $27MHz$, $g << \lambda/4$. The largest dimension of the transceiver system is $A_x = 150\ mm$, which is $<< \lambda/2\pi = 1767mm$ at target frequency of $27MHz$. Thus, the proposed receiver in its present form is electrically small[S1,S2].

It has been observed that the dimensions of the lumped RLC elements become the part of the over all electrical length of the antenna beyond $900MHz$[S3,S4]. However, in the HF regime, the dimensions of the RLC elements can not provide the appropriate electrical length. Electrically small antenna's have poor radiation efficiency, which in turn also

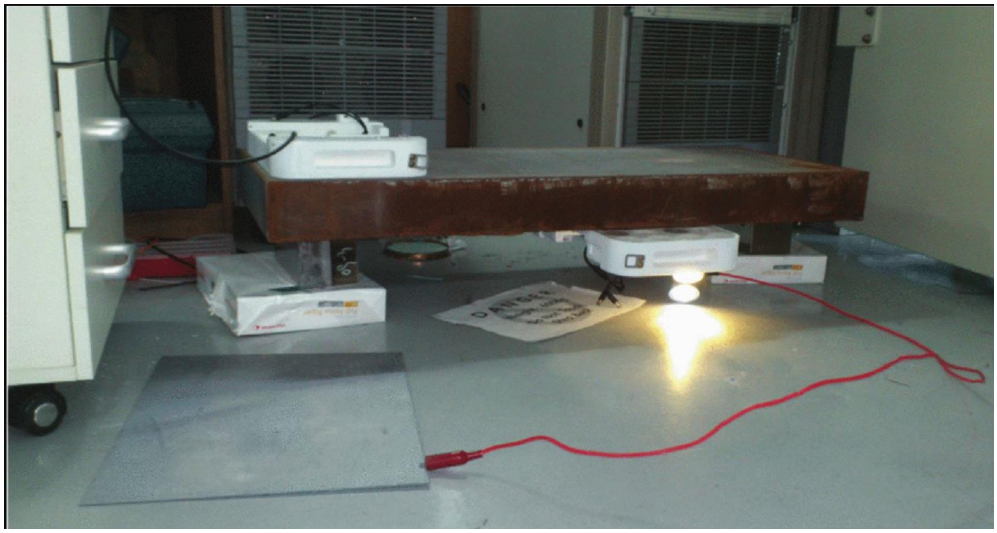

Fig. S 1 – Earlier experiments: Power transfer across 80 mm using the ground-wire counterpoise on the receiving unit to sustain voltage oscillation

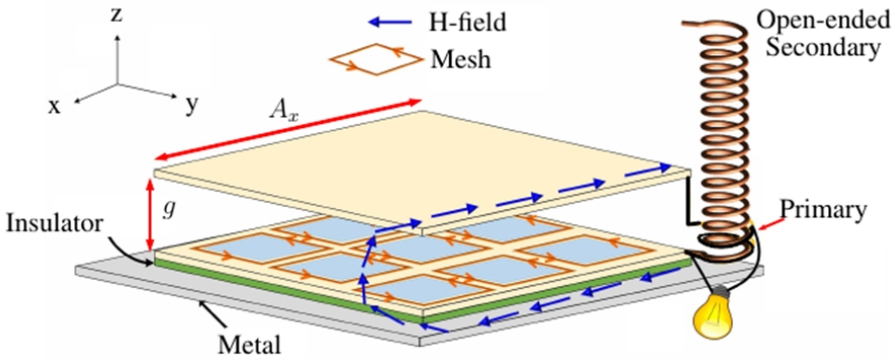

Fig. S 2 – Schematic of the proposed resonator system

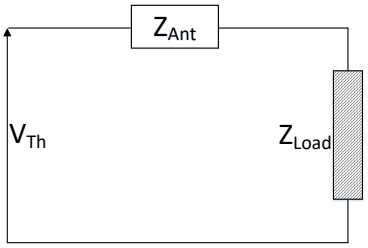

Fig. S 3 – Thevenin voltage across the antenna terminal

hinders the receiving capabilities of high frequency antennas[S1,S2]. However, the radiation efficiency of the receiving antennas can be improved.

We will now derive the expression for radiation efficiency η. As per the standard definition of electrically small antennas, the wave number k and a spherical radius, a, in space is related to wavelength λ[S1,S2]:

$$ka = \frac{2\pi}{\lambda} \tag{S1}$$

Where, the radius a happens to be the largest dimension of the antenna[S1]. The following analysis can be applied to mono pole and multi-turn helical loop antennas, alike. The quarter wavelength counterpoise is like a mono pole, hence we will leave out monople and focus on multi-turn helical coils. The radiation resistance is related to the area, A_{loop} of a helical loop of N turns by[S1,S2]:

$$R_{rh} = 320\pi^2 N^2 \left(\frac{A_{loop}}{\lambda^2}\right)^2 \tag{S2}$$

Generalized expression for received power in any antenna, in terms of power density $P_d[Watts/m^2]$, mismatch loss τ , antenna efficiency and directivity D is given by:

$$P_{received} - P_d \tau \eta \frac{\lambda^2 D}{4\pi} \tag{S3}$$

From the equation S2 one can notice that, loop antenna is less efficient as transmitter[S1]. However, it can be an excellent receiving antenna[S2], because the radiation resistance increases by a factor of N^2 . Consider a simplified circuit model of the antenna in S.3, the thevenin voltage across the terminals of the antenna can be determined. The mismatch loss τ can be related with antenna resistance $R_{Ant} = R_{Loss} + R_{rh}$, antenna impedance Z_{Ant} and load impedance across the antenna feed-point, Z_{Load} :

$$\tau = \frac{4R_{Ant}R_L}{|Z_{Ant} + Z_{Load}|^2} \tag{S4}$$

For antennas operating in the resonance frequency, the radiation and loss resistances are modeled as series. The corresponding Thevenins voltage is given by:

$$|V_{Th}| = \frac{|E|\lambda}{\pi}\sqrt{\left(\frac{R_{rh}D}{120}\right)} = \frac{|E|\lambda}{\pi}\sqrt{\left(\frac{\eta R_{Ant}D}{120}\right)} \tag{S5}$$

From the equation S5, the efficiency η can be related to radiation resistance and antenna resistance as:

$$\eta = \frac{R_{rh}}{R_{Ant}} \tag{S6}$$

Based on the above aspects, the authors identified the quarter-wave length section of wire as one of the earliest alternatives to the ground plate-wire counterpoise. One such reading of current and voltage values along the length of the quarter wavelength wire counterpoise is listed in table 1.

Table ST 1 – Current and voltage across the counterpoise

Length	DC RMS Current (mA)	DC RMS Voltage (V)
$\frac{1}{3}(\lambda/4)$	360.74	13.0515
$\frac{2}{3}(\lambda/4)$	362.5	22.19
Full Length ($\lambda/4$)	361.1	43.82
Tx side	1200	56
Rx terminals	796	12

The increase in the voltage across the length of the wire made sense, this agrees with the equations S1-S6. However, the physical dimensions of such a counterpoise would make the system unfeasible for practical applications. In order to increase the radiation resistance and receiving efficiency, the logical choice would be a multi-turn helical coil. Attaching an electrical conductor to one of the copper elements of the GBI resonator would simply change the resonance conditions[S5,S6]. In order to prevent the change of resonant conditions and to drive the reference voltage of the GBI structure to a high level, the half wave helical coil was incorporated in the tesla transformer fashion.

1.1 Quarter-Wave or Half-Wave Helical transformer?

The secondary of the Tesla transformers are essentially quarter wave coils which generate standing waves. In our report we demonstrate that half-wave helical coils stand as an

alternative to tesla transformers. The self resonance of these coils can serve as an effective means to determine the resonance frequency. Tesla transformer "like" arrangement can oscillate the voltage and current levels across the terminals. These findings are listed in table ST4. To our understanding the half-wave helical coils can not generate standing waves.

2 Experimental results

The Fig.S 4 A and B shows the proposed resonator system, containing the GBI structure and Tesla transformer like half-wave length helical coil. The Fig.S 4 C, shows measured values of the E-field attenuation along the Y-axis(E_z component as a function of Y, denoted by $E_z(Y)$), along the metal-air interface. The height of the receiver(Rx) is fixed at $Z = 0.001m$ and moved along the Y-axis to record the E-field intensities. These values were obtained using the state-of-the-art spectrum analyzer. The transmitter is fed with an input power of 0 dBm. The E_z values are shown in $dB\mu V/m$ scales. Two resonators with frequencies 27 and 36 MHz is used for the measurement. It is observed that, the attenuation rate is slow and independent of the frequency[S7,S8]. The frequency independent slow attenuation rate of E-fields is the hallmark of the Zenneck waves[S7–S10]. The Fig.S 4 D, shows the measured values of the transmittance parameters along the Z-axis or the vertical direction away from the metal surface. The scales shown for the transmittance are in log magnitude. It is observed that in the linear scale, the transmittance decay is exponential in nature. This implies that the excited wave shows the well-known evanescent property of the Zenneck wave ([S7–S10]). The Fig.S 4 E, shows the measured values of transmittance when the transmitter (Tx) is placed inside an aluminum metal shield of dimension:400mm $\times$ 350 mm $\times$300 mm. The gap between metal and the shield was set at 7.5 mm, mimicking the gap left by the neoprene gaskets in the case of ship containers. It is observed that unlike coupled WPT systems, the metal shield does not cause the peak shifting or degradation of transmittance values[S11,S12]. The Fig.S 4 F, shows the measured efficiency extracted from the transmittance parameters by the relation $|S21|^2$ for two receiving units over a distance of 8 m along the metal surface. It is observed that there is no change in the values of power transfer efficiency for the case of mis-aligned Tx and Rx.

3 Simulations

The Fig.S 5 A, shows the numerical simulation of E-field profiles when the Tx is housed inside the partial aluminum shield. The Fig.S 5 B, shows the case when there is no shield. It is observed that there is a slight degradation of the intensity of the modes when the shield

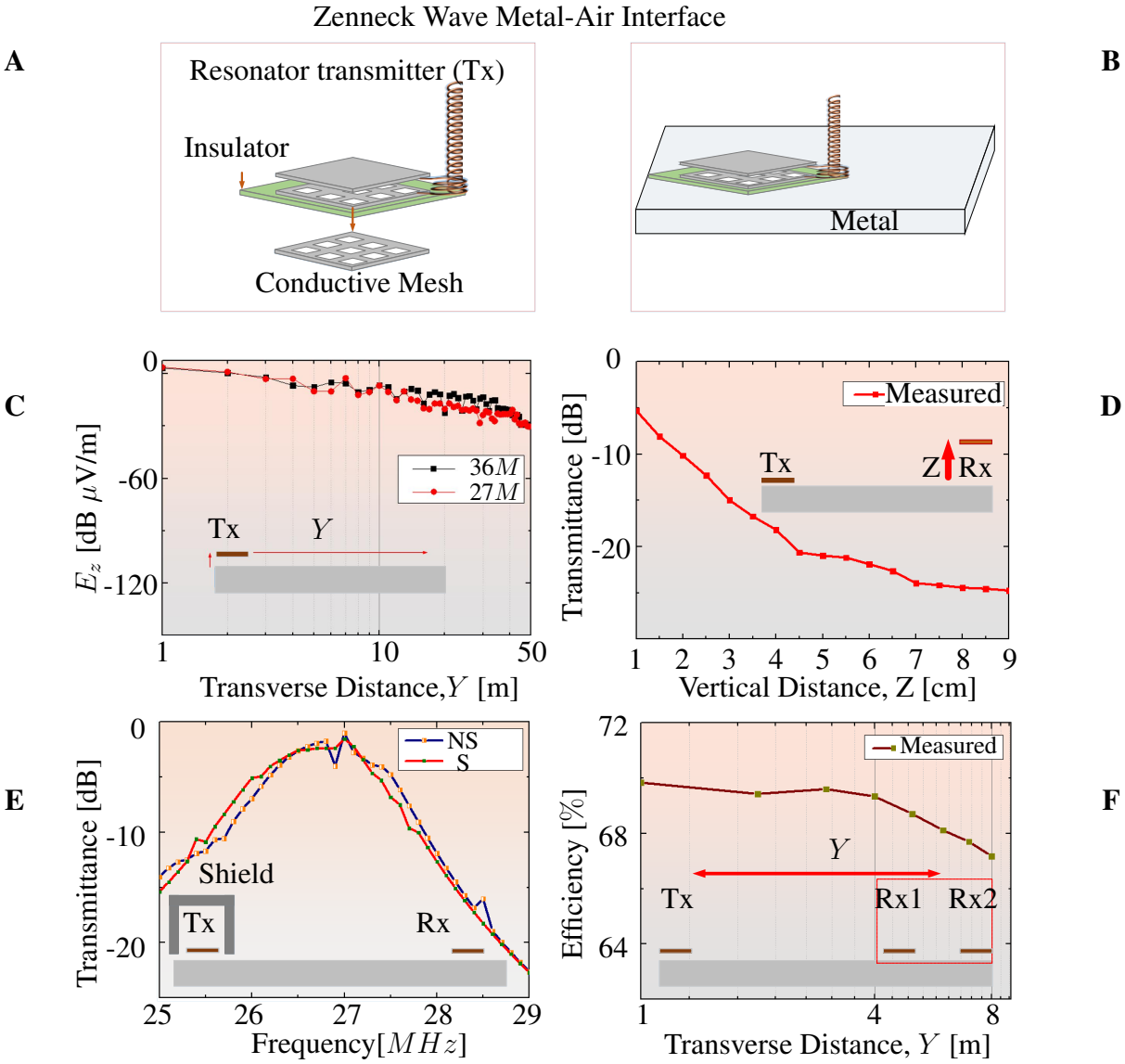

Fig. S 4 – Experiment to excite Zenneck Wave at metal-air interface (A) Ground Backed Impedance resonator system, with a half wavelength helical coil. (B) Placed on the metal surface with electrical isolation.(C) Experimental results of the Z component of the Electric field in the Y-direction 1 to 50 m, shows a slow attenuation rate. (D) Evanescent field decay experiment.(E) Experimental results of the transmittance parameters, when transmitting and receiving unit are under shield and no-shield conditions. (F) Multi receiver power transfer efficiency.

is applied. The Fig.S 5 C, shows the case when the first half along the Y axis is a metal-air interface and the second half is a lossy dielectric-air interface. It is observed that the modes are curved backwards in the metal-air interface. This is due to the difference in the group velocities in the air and metal. The wave travels faster at the edges of the metal than compared to air. On the other hand, when a lossy dielectric-air interface is encountered, the modes change their curvature and are tilted forward. The free-space velocity is higher as compared to lossy dielectric. The Zenneck wave simply sinks into the dielectric media. These results are diagrammatically listed in the Fig. S 5 D, we find these properties to be in accordance with the mathematical model presented by Barlow and Cullen in their classic 1953 article[S10]. Specifically figure 7 A of their article. Likewise, a similar property was numerically and experimentally observed by[S13]. They observed the sinking property of the zenneck wave into a dielectric media as well. However, they used a metasurface-air interface to launch the Zenneck waves[S13].

The Fig. S 5 E, shows the simulated transmittance parameters of the helical coil placed at different heights of 105 mm and 260 mm. It is observed that the height adjustment of the helical coil above the ground layer of the antenna optimizes the transmittance parameters. The primary of the helical coil carries current, the resultant magnetic field causes eddy currents when close to the metal or the ground layer of the GBI resonator. The Fig.S 5 F, shows the attenuation of the $E_z(Y)$ for the cases of aluminium-air, iron-air and seawater-air interfaces. It is observed that the attenuation is slightly more pronounced for seawater-air interface. This may be reasoned to the fact that seawater is diamagnetic in nature. Fig. S 6 A, shows the measured and simulated results of the E-field attenuation along the aluminium-air interface at 27 MHz. The height of the Rx is fixed at $Z = 0.001m$ It is observed that the simulation and experiment are in good agreement. Fig. S 6 B, shows the measured and simulated efficiency plot for the case of multiple receivers. The theory and experiment are in good agreement. More details on power transfer metrics are presented in the supplementary material. Fig. S 6 C, shows the simulated and measured transmittance parameters for shielding and no shielding. The inset view shows the flattening of the resonance peak when the shield is applied, span of the bandwidth was 0.75 MHz. It is possible to use this entire span for the power transmission, with uniform efficiency. Fig. 6 D, shows the experimental and simulation plot of the decay of transmittance parameters in the vertical direction away from the metal surface, in the log scale. It is observed that the transmittance parameters decay exponentially, in accordance with the Zenneck wave properties[S7–S10].

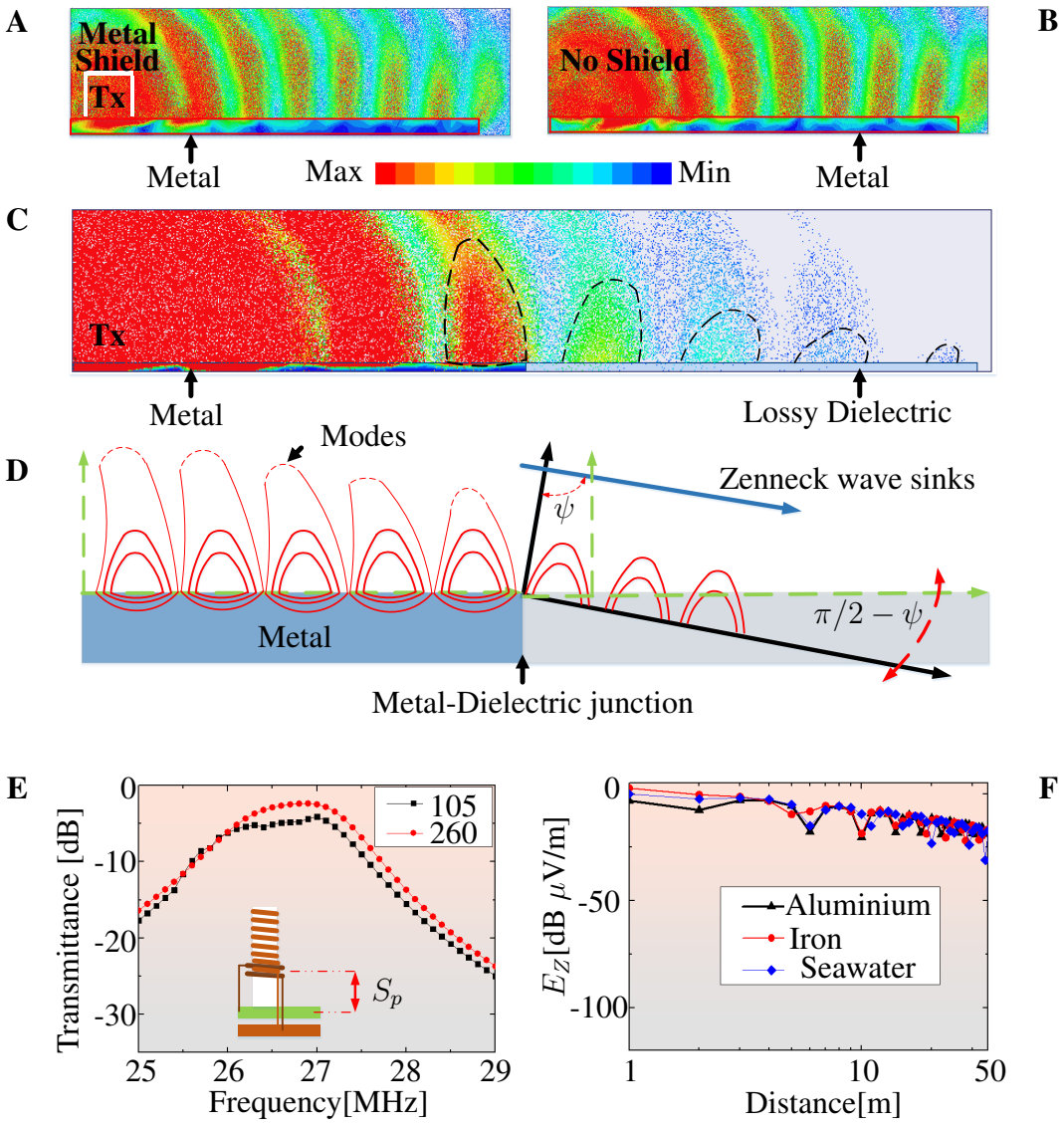

Fig. S 5 – FEM Simulation Model. (A) E-field mode excitation, when transmitter(Tx) housed inside a partial metal shield. (B) E-field mode excitation when there is no shield. The Tx is electrically isolated from the metal at all times. (C) E-field mode excitation when the first half is metal and the other half is a lossy dielectric with ϵ_r=4. (D) Representative diagram of the mode profiles, completing in free space. The Zenneck wave sinks into the lossy dielectric. (E) Transmittance parameters when the coil is placed at a vertical spacer of S_p =105 mm and 260 mm from the ground layer of the resonator. (F) Attenuation of E-field in the transverse direction along the interface of Air-Aluminium, Air-Iron, Air-Seawater.

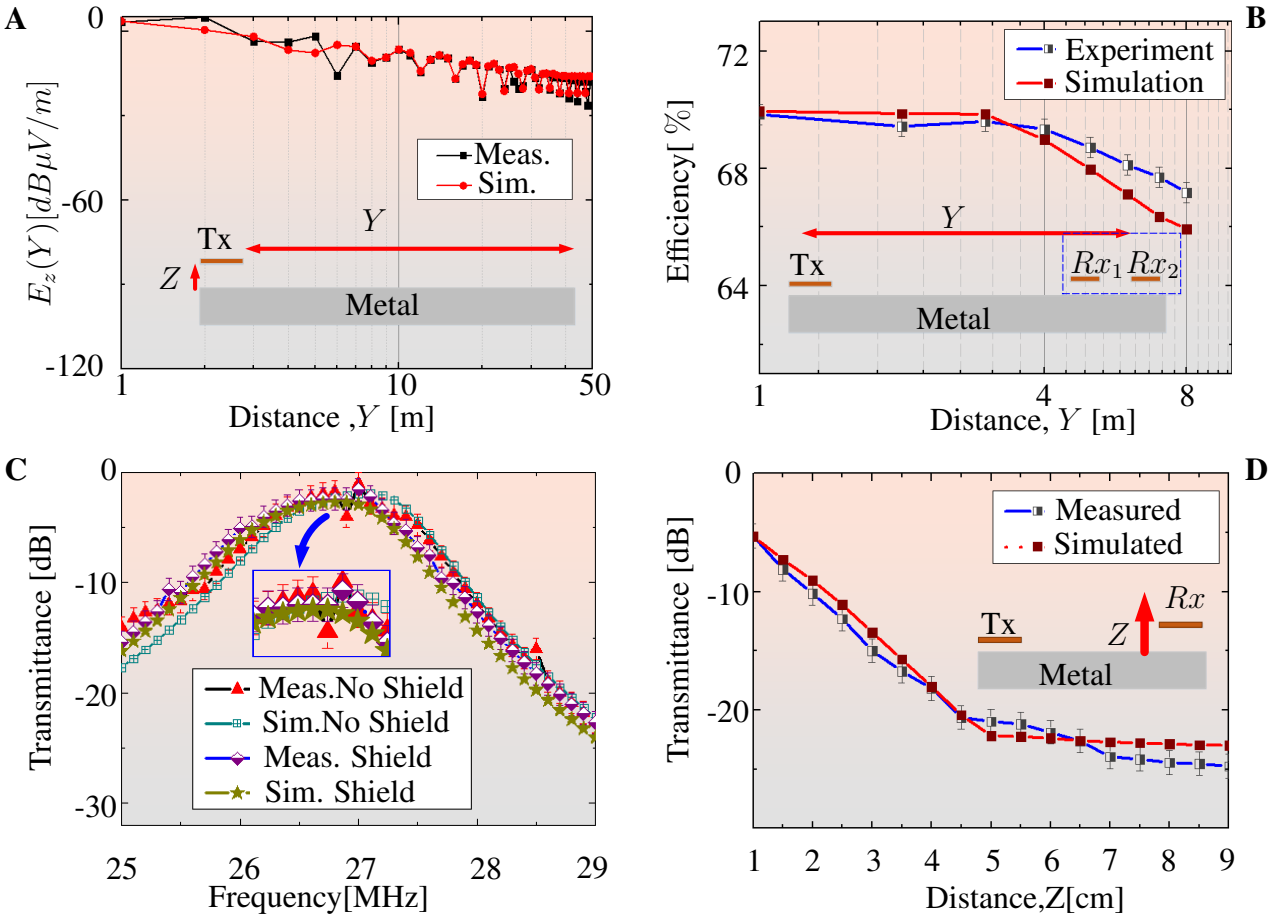

Fig. S 6 – Measured and Simulated (A) E-field attenuation along the transverse direction of metal-air interface: $E(Y)$, $Z = 0.01mm$ for $27MHz$ design. (B) Two receiver efficiency. (C) Transmittance parameters under shielded and no shield conditions. No frequency shift was observed. However, flattening of the peak occurred. Thus, forming a bandwidth of 0.85 MHz. (D) Transmittance decay along the Z direction, exhibits an evanescent property. Please note, the transmittance is in log scale.

3.1 Multi-receiver characteristics Comparison with coupled systems

The Fig. S 7 A and B show the well noted frequency splitting phenomena in case of coupled WPT systems. Whereas, the Fig. S 7 C and D, show the case of the proposed Zenneck Wave based WPT system, the power is uniformly received across both the receivers.

4 Analytical Formalism: Vertical and Horizontal Hertz dipole over metal-planes

Retaining the notation as suggested by Sommerfeld[S14]; let ω be the frequency in radians, $k = 2\pi/\lambda = \omega/c$ be the wavenumber and c be the speed of light. Their corresponding relation with the Hertzian potential:

$$\prod = \frac{1}{r} e^{i(kr-\omega t)} \tag{S7}$$

From the electrodynamics point of view, Hertzian potential is a vector and now on shall be denoted by $\overrightarrow{\prod}$. The proposed system is electrically small and hence, the current carried by the antenna has no phase variations on the primary side of the helical coil and the GBI structure. Please note, there will be no current carried by the secondary helical coil, as it is in principle an open-circuit. As shown in Fig. S 8, the interface between metal and free space exists as $Z = 0$. The tangential E field component would be zero in accordance with Maxwell's equation[S8]:

$$(k^2 . \overrightarrow{\prod} + grad\ div \overrightarrow{\prod})_{tang} = 0 \tag{S8}$$

This is satisfied by combined effect of the dipoles with their corresponding mirror images formed in the metal as shown in the Fig. S8. Sarkar et al. also used Schelkunoff integrals for images formed in imperfect earth[S8,S9]. Evidently, there are two kinds of dipoles which need to be considered in the case at hand.

1. Vertical dipole, originating from the primary coil at a distance h above $z = 0$. Leading to expression for the vector potential:

$$\prod = \prod_z = \frac{e^{ikR}}{R} + \frac{e^{ikR'}}{R'} \begin{cases} R^2 = r^2 + (z-h)^2, \\ R'^2 = r^2 + (z+h)^2. \end{cases} \tag{S9}$$

   In the Fig. S8, the term HUC_v denotes the hypothetical unit charge at $Z = 0$, thus resulting to a force in the Z direction. The $E_{tang} = 0$.

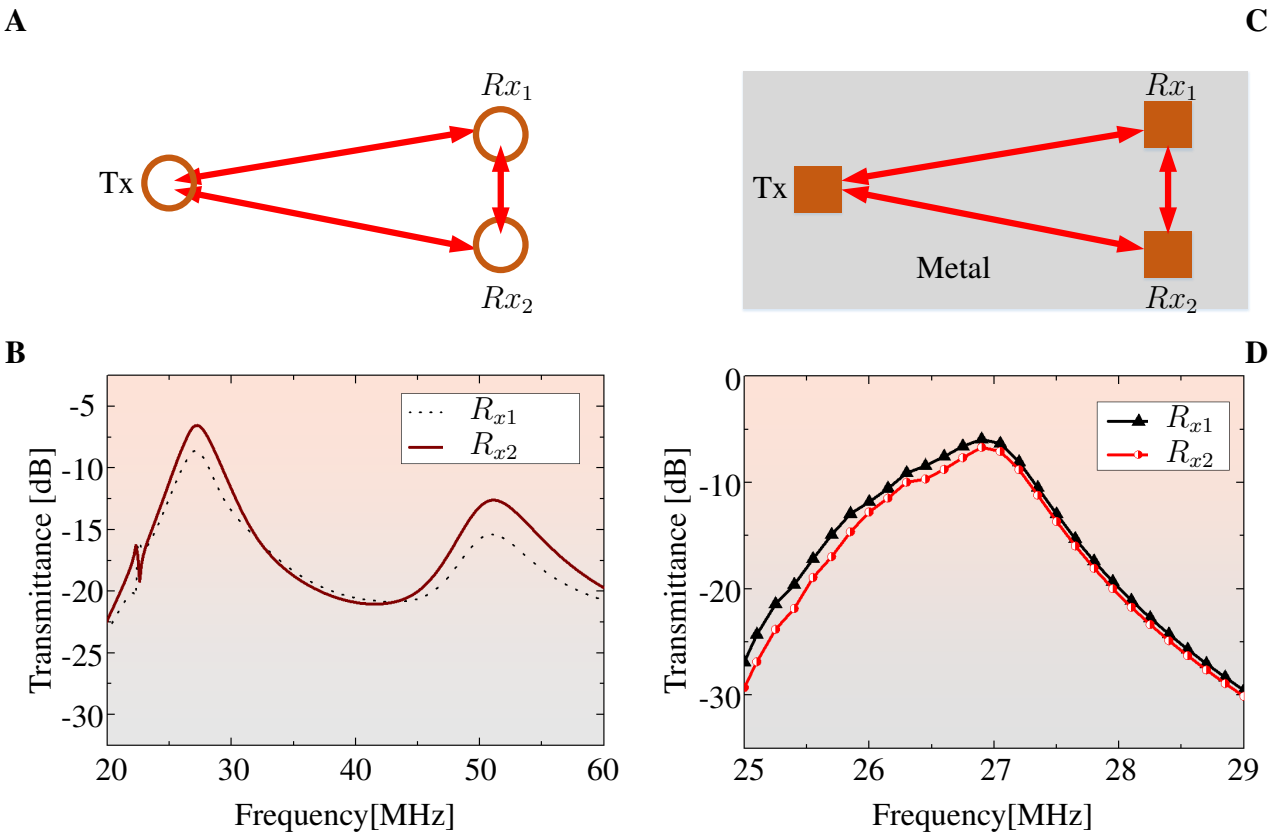

Fig. S 7 – Simulated (A) Inductively coupled WPT system. (B) Inductively coupled Transmittance parameters for multiple receivers. Frequency splitting is observed, when both the receivers are in proximity. (C) Zenneck Wave WPT system. (D) Zenneck Wave Transmittance parameters for multiple receivers. No frequency split and uniform power transfer is observed.

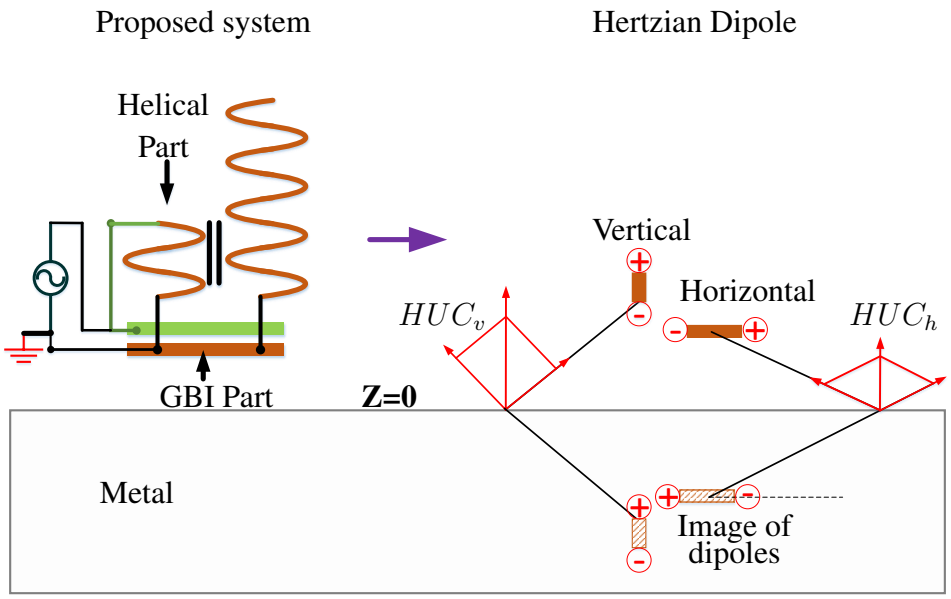

Fig. S 8 – Reflection by a metal surface, the proposed system can be viewed as a combination of vertical and horizontal dipole.

2. The Horizontal dipole arising from the GBI structure can be expressed by:

$$\prod = \prod_x = \frac{e^{ikR}}{R} - \frac{e^{ikR'}}{R'} \tag{S10}$$

The horizontal dipole forms a hypothetical unit charge, denoted by HUC_h, resulting into a force in the Z direction and thus causing the $E_{tang} = 0$.

3. If one applies a limit $h \to 0$, then the vertical dipole results in a $\prod = 2.e^{ikR}/R$, while horizontal dipole's vector potential vanishes. In the present case, we have placed the resonator system at a distance of $h = 0.001mm$. Its, contribution to the directional characteristic is considered for the final evaluation.

4. Therefore, the generalized forms of the equations S9 and S10, with amplitudes A and B can be expressed as:

$$\prod = \prod_z = A.\frac{e^{ikR}}{R} \tag{S11}$$

The horizontal dipole can be expressed as a quadrupole as:

$$\prod = \prod_z = B.\frac{\partial}{\partial x}\frac{e^{ikR}}{R} \tag{S12}$$

The complex refractive index n for the metal is related as:

$$n = \sqrt{\frac{1}{\epsilon_0}(\epsilon + i\frac{\sigma}{\omega})} \tag{S13}$$

where σ is the conductivity and ϵ_0 and ϵ are the free-space permittivity and relative permittivity, respectively. The wavenumber in the free-space (k) and the metal (k_M) can be related as:

$$k_M = nk \tag{S14}$$

4.1 Three regions in the interface

The height of the location of the Hertzian dipole is denoted by h as mentioned earlier. There are three distinct regions to be considered for the analysis.

4.1.1 Region-I: $z > h$ (Metal-Air interface)

In the analysis by Sommerfeld on the problem of dipole over arbitrary ground with finite conductivity, it was assumed that in addition to a primary stimulus originating from the antenna at $r = 0$ and $Z = h$, there exists a secondary stimulus, due to localized charge oscillations in the earth. Dealing with the problem in the cylindrical polar coordinates (r, ϕ, z), we shall use the eigenfunctions u and eigen values Λ. Applying similar analogy to the case of metals we can arrive at the following relations:

$$\begin{aligned} \prod_{prim} &= \int_0^\infty j_0(\Lambda r) e^{-M(z-h)} \frac{\Lambda d\Lambda}{M} \\ \prod_{sec} &= \int_0^\infty F(\Lambda) j_0(\Lambda r) e^{-M(z-h)} d\Lambda \end{aligned} \tag{S15}$$

Where, $F(\Lambda)$ is the undetermined spectral distributions in the Λ-continuum of the eigenfunctions. The quantity, j_0 is the Bessel's function. The quantities $u = j_0(\Lambda r) \cos Mz$ and $k^2 = \Lambda^2 + M^2$.

4.1.2 Region-II: $h > z > 0$ (Air)

The primary and secondary stimulus exists in this case as well, represented by the analytical relations similar to S15:

$$\begin{aligned} \prod_{prim} &= \int_0^\infty j_0(\Lambda r) e^{+M(z-h)} \frac{\Lambda d\Lambda}{M} \\ \prod_{sec} &= \int_0^\infty F(\Lambda) j_0(\Lambda r) e^{-M(z+h)} d\Lambda \end{aligned} \tag{S16}$$

The equations S15 and S16 follow continuity behaviour of the $\prod$ field at the boundary for an arbitrary $F(\Lambda)$.

4.1.3 Region-III: $0 > z > -\infty$ (Metal)

There would be no primary stimulation in this case; the field denoted by $\prod_M$ must be continuous throughout.

$$\prod_M = \int_0^\infty F_M(\lambda) j_0(\Lambda r) e^{+M_M z - Mh} d\Lambda, \qquad M_M^2 = \Lambda^2 - k_M^2. \tag{S17}$$

The equations S16 and S17 satisfy the maxwells boundary conditions of continuity, their resulting relation would be(region II and region III):

$$\int_0^\infty j_0(\Lambda r) e^{+M(z-h)} \frac{\Lambda d\Lambda}{M} + \int_0^\infty F(\Lambda) j_0(\Lambda r) e^{-M(z+h)} d\Lambda = n^2 . \int_0^\infty F_M(\lambda) j_0(\Lambda r) e^{+M_M z - Mh} d\Lambda \tag{S18}$$

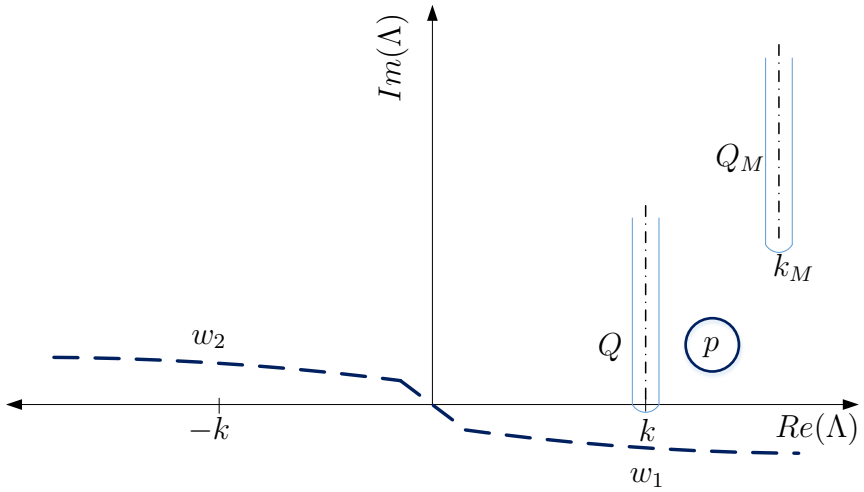

Fig. S 9 – Integration paths w_1 and $w = w_1 + w_2$, the path deforms around the branch-cuts Q, Q_M and the pole p.

The first term on the LHS of the equation S18 is the $\prod_{prim}$ and the second term is $\prod_{sec}$ from the equation S16. The RHS is the S17 multiplied by n^2 which comes from equation S13. Solving the above equations in the complex plane as shown in Fig. 9, results in the four Riemann sheets($\Lambda = k$ and $\Lambda = k_M$) and simplifying in their bessel function form, we get the Hankel function of type 1 and 2:

$$j_0 = \frac{1}{2}(H_0^1 + H_0^2) \tag{S19}$$

Substituting $\varrho = \Lambda r$ the equation S19 becomes:

$$j_0 = \frac{1}{2}(H_0^1(\Lambda r) + H_0^1(\Lambda e^{i\pi} r)) \tag{S20}$$

Notice, only the Hankel function of the first type remains. Integration through the path w_1 and w_2, we obtain the following integral:

$$\int_{W_1} j_0(\Lambda r) f_{arb}(\Lambda^2) \Lambda' d\Lambda' = \frac{1}{2} \int_W H_0^1(\Lambda r) f_{arb}(\Lambda^2) \Lambda d\Lambda \tag{S21}$$

Where, $f_{arb}(\Lambda^2)$ is an arbitrary function of Λ^2. Thus, the real integral has been converted into a complex integral closing at infinity. Thus the solution for the primary stimulation:

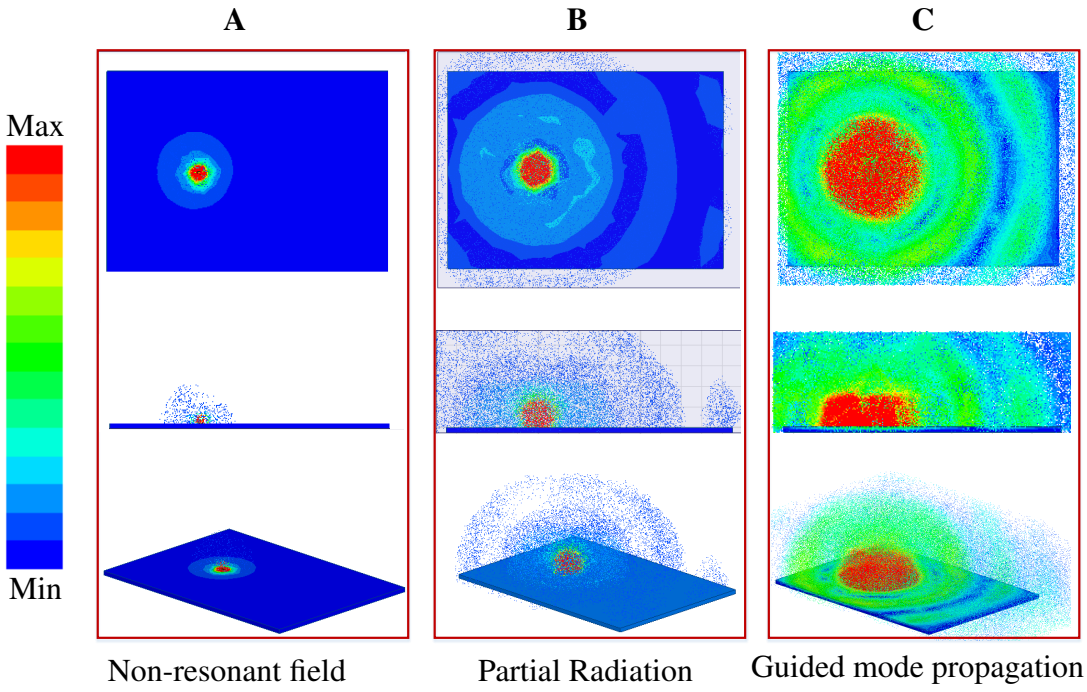

Fig. S 10 – Superposition of fields: (A) GBI resonator a case of horizontal dipole (B) Half-wave Helical coils as a case of vertical dipole (C) Proposed system, a combination of GBI and Half-wave Helical

$$\prod_{prim} = \frac{1}{2}\int_{w} H_0^1(\Lambda r)e^{-M|z|}\frac{\Lambda d\Lambda}{M} \tag{S22}$$

$$\prod = \int_{w} H_0^1(\Lambda r)e^{-Mz}\frac{n^2\Lambda d\Lambda}{n^2M + M_M} \tag{S23}$$

It is evident from the fig. 9,in the positive imaginary half plane, the Hankel function of the first order $H^1(\Lambda r)$ vanishes at infinity. The path of integration avoids the loops Q and Q_M. The singularity exists for integrand as shown in equation S23, the denominator $n^2M + M_M$ would vanish at:

$$\Lambda = p$$

We have three components Q,Q_M and p, the contribution of Q_M can be safely ignore for the large values of $|k_M|$ because the Hankel function decays exponentially at large distances from the real axis. By applying method of residues and setting up the relationship

$\widetilde{K} = k_M^2/(\sqrt{p^2-k^2}) + k^2/(\sqrt{p^2-k_M^2})$ one arrives at the following new relations for the vector potential:

$$\prod = 2\sqrt{2\pi i/pr}\frac{k_M^2}{\widetilde{K}}e^{ipr-\sqrt{p^2-k^2}z}, \qquad z \geq 0, \tag{S24}$$

$$\prod_M = 2\sqrt{2\pi i/pr}\frac{k^2}{\widetilde{K}}e^{ipr+\sqrt{p^2-k_M^2}z}, \qquad z \leq 0, \tag{S25}$$

Finally the above equations can be written in a modified form for a wave in direction of the negative x-axis:

$$\prod = A.k_M^2 e^{ipx-\sqrt{p^2-k^2}z}, \tag{S26}$$

$$\prod_M = A.k^2 e^{ipx+\sqrt{p^2-k_M^2}z} \tag{S27}$$

Where, A is a slowly varying amplitude factor, the equation S26 and S27 describe the Zenneck waves, which were originally proposed by Jonathan Zenneck in 1907.

The Fig. S 10, shows the resulting field profiles to justify the analytical equations S7-S27. In Fig. S 10 A, it is observed that the GBI resonator displays a very weak TM-field. This seems to be in-line with the analytical equation S10, when the limit of $h \to 0.001m$ is applied. This has also been analyzed by the use of Schelkunoff integrals by[S8,S9]. The Fig. 10 B, shows the field profile over a finite metal, when the helical coil is placed at a $h = 0.26m$. It is observed that the helical coil displays properties in-line with the analytical equation S9. Also, the helical coil happens to be a bad radiator, evident from the simulated field profile. The combined effect of horizontal and vertical Herztian dipole is seen in Fig. 10C, which is method undertaken in this study to excite the Zenneck waves, shows a propagated mode. We have also seen this in Fig. 3 of the main document.

5 How is metal a neutral entity in the proposed system?

The neutral character of metal in the presented case is of critical importance, keeping in mind the safety of the operator. As per the standard definition the electric current is the rate of change of charged particles across a unit cross section or flow of charged particles in a medium. The Fig.S 11 A and B shows the simulation of the field profiles in their contour and vector format. The Fig.S 11 C shows the diagrammatic view of the direction of the vectors. The field lines extend into the air from the interface to a large distance(in the order of λ), however most of the field lines will be confined in the vicinity of the interface[S15–S19]. The field lines in metal will extend comparatively to a lesser depth(order of skin-depth)

and will be in the same phase as that of the field lines in the air. From the Fig.S 11 B and C, it can be understood that the field modes are localized at the interface, hence, the net flow of charge is zero.

Table ST 2 – Coil details for Transmitter and Receiver

Parameter	Specifics
Secondary turns	52
Radius Secondary	18 mm
Primary Turns	2
Radius Primary	20 mm
Coil pitch in primary and secondary	4.3 mm
Coil to Rx ground spacer	230 mm
Secondary Coil Inductance	13.2 μH
Secondary Coil self capacitance	3.315 pF
Primary Coil Inductance	0.104 μH
Primary Coil self capacitance	1.208 pF

6 ICNIRP field compliance

One of the critical questions is the occupational hazard exposure from the proposed system, if used on board marine vessels, smart shipping containers and home IOT device charging. Therefore, it was necessary to test the international commission for non ionizing radiation protocol compliance of the proposed system. The state-of-the-art Narda field measurement analyzer was used to record the E and H-field values across the spectrum of $1MHz$ to $30MHz$. The power fed into the transmitter was 65 $watts$. The fig.S 13 shows one of the several chosen position of the probe, which recorded maximum field intensities at the receiver and the edge of the metal. Fig.S 14, shows the recorded values of the Narda field test analyzer measurements. As per the ICNIRP regulation, between 10 MHz and 400 MHz the maximum permissible value of E -field is 61 V/m[S20]. The maximum permissible regulatory value for H-field 0.16 A/m. The measured values of E and H-field in the proposed system is 40.3 V/m and 0.018 A/m, respectively, at $13.3MHz$. Implying,

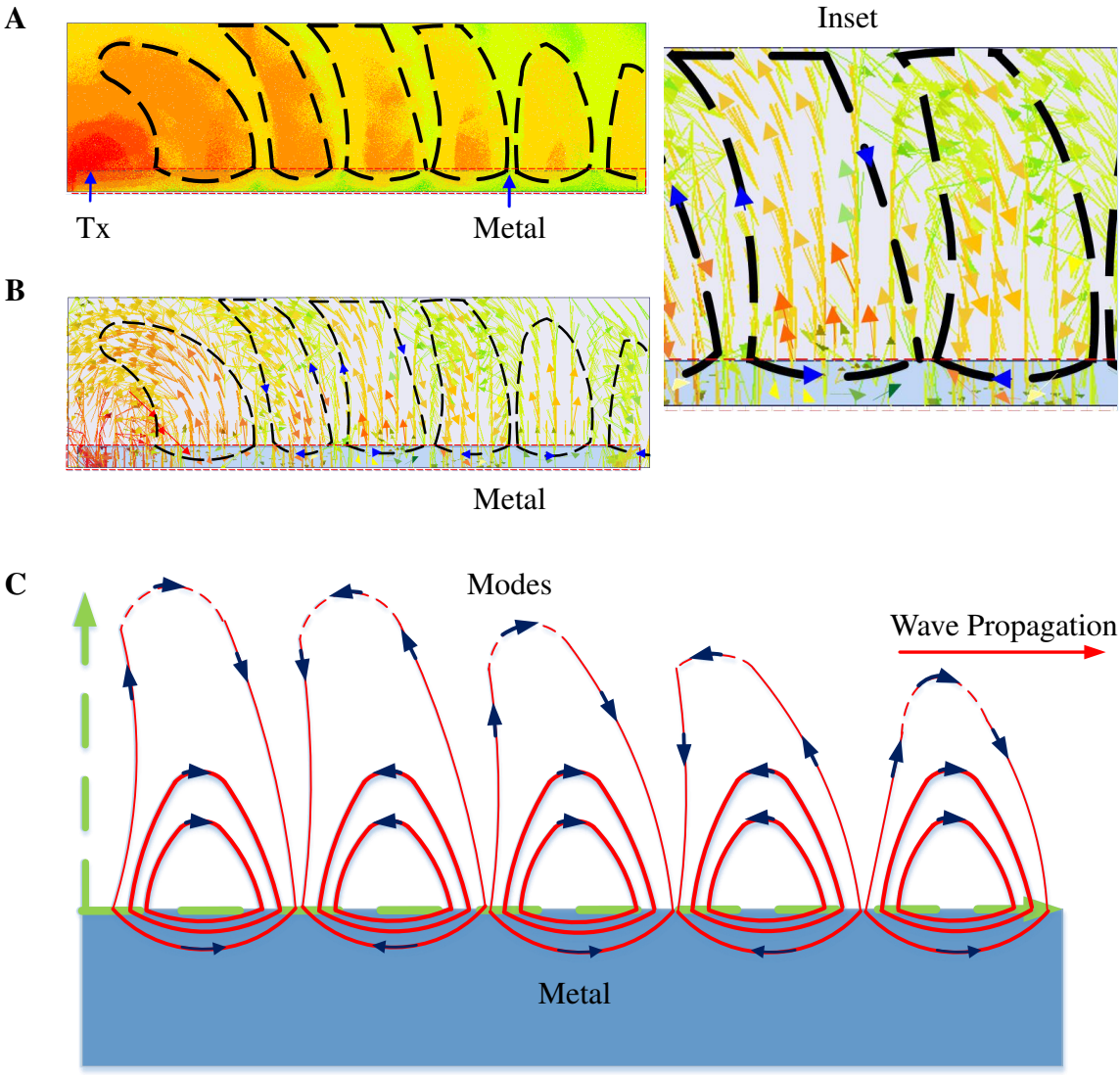

Fig. S 11 – Metal as a neutral entity: FEM simulation of Localized charge oscillation (A) Contour Plot of E-field modes at metal-air interface(B) Vectored plot of E-field modes at metal-air interface. (C) Diagrammatic representation of Zenneck Wave E-field vectors compared with the inset view of the simulation. The charged particles do not flow, therefore current does not exist in the metal.

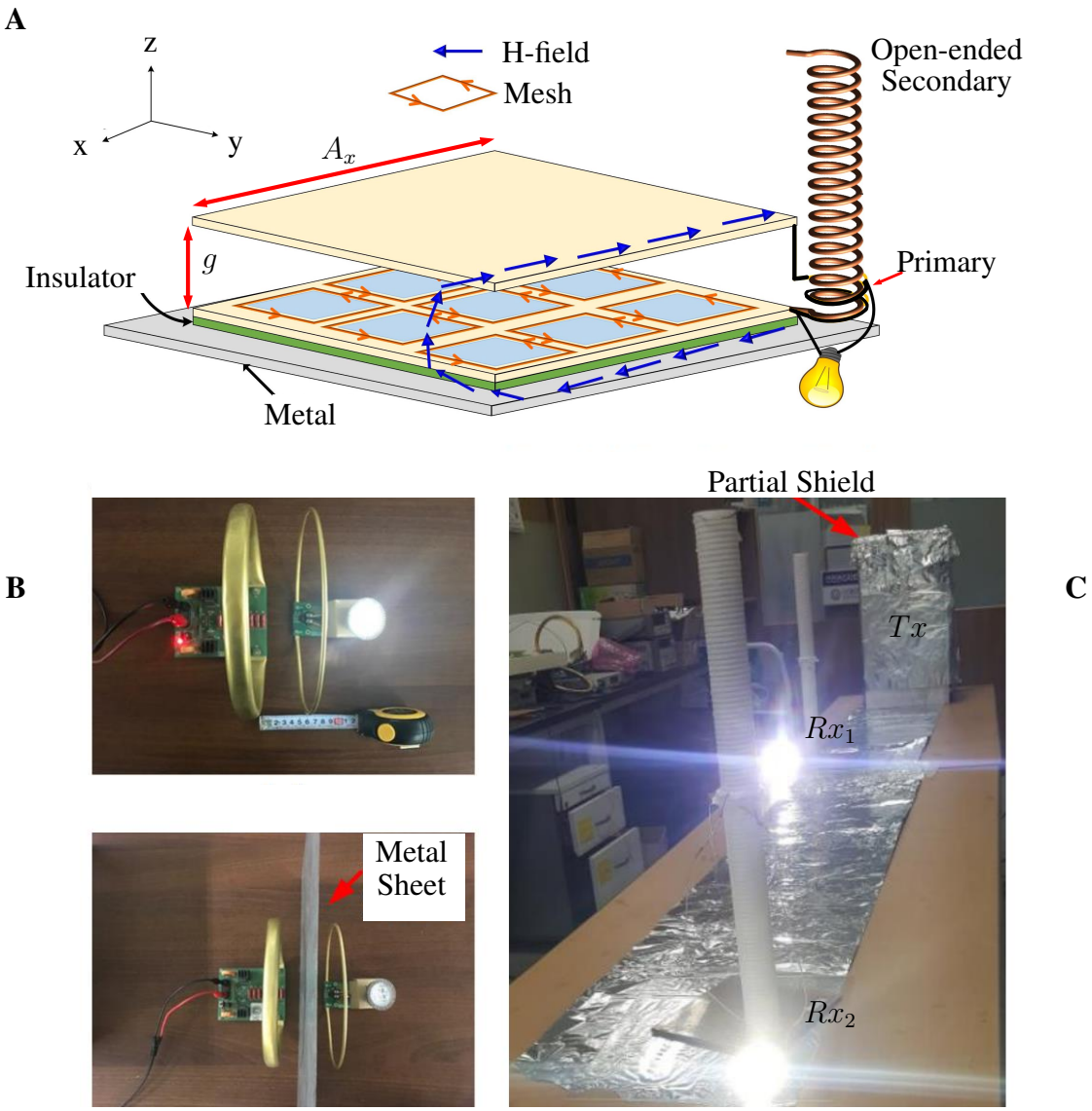

Fig. S 12 – Schematics and Demonstration (A) The receiver schematic diagram with load connected across the GBI structure's terminals $A_x = 150mm$,$g = 1.5mm$, $mesh\ slot = 30mm \times 30mm$; (expanded view of GBI) (B) EM shielding: Inductively coupled power transfer system under a plane metal sheet (C) Proposed Zenneck wave system, transmitter housed inside a partial shield illuminating multiple receivers Rx_1 and Rx_2

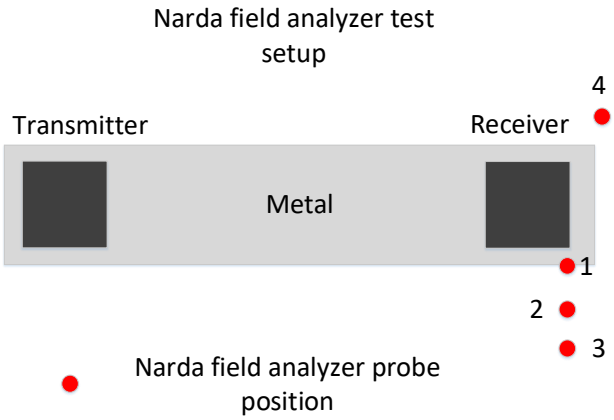

Fig. S 13 – Measurement setup for ICNIRP field compliance test. The red circles show the positions of the isometric probe of the field analyzer for measuring the field intensities.

that the proposed system generates a maximum E-field of 33.9 % and H-field of 88.7 % lower than the regulation. Hence, the proposed system is safe for operation for human operators[S20].

Table ST 3 – Recorded E and H field results

Position	E $[V/m]$	H $[A/m]$	Details
1	40.3	0.018	2 mm vertical distance from metal
2	17.09	0.06803	100 mm horizontal
3	11.04	0.0205	150 mm horizontal 150 mm vertical from metal
4	19.7	0.073	100 mm corner from metal

Table ST 3 lists the recorded field intensity values at various positions. The highest field values are recorded at the position 1 as shown in fig.S 13. The lowest is observed at position 3. A slightly higher value as compared to position 2 and 3 is observed at position 4. This slight rise in value can be attributed to the radiating power at the sharp corners of the metal. Its noteworthy, that the input power into the transmitter was kept at a higher value (65 $watts$) than the intended power value of 50 $watts$ for household usage. When two receivers are used, the value of E and H fields drop significantly below the public exposure regulations[S20].

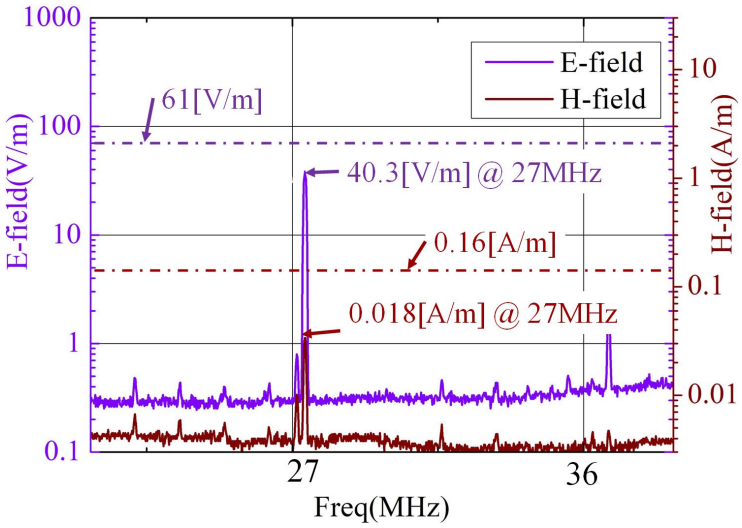

Fig. S 14 – Recorded EM fields for position 1 using a Narda STS EHP-200A Electric and Magnetic Field Analyzer; the solid lines represent the measured values, the dashed lines the regulatory reference(61V/m and 0.16 A/m)

6.1 Power transfer metrics

The table ST 4 summarizes the power transfer efficiency metrics. As can be seen, the helical coil transformer arrangement, as a counterpoise, significantly improves the power transfer efficiency. The transmitter was fed with a power amplifier as a source. The table ST 5 lists the voltage and current metrics across the various counterpoise systems considered in this work. Both the quarter wave length wire and the ground plate-wire counterpoise had to be left touching the earth ground. Therefore, a current return path used to form from the receiver to the source. Hence, there exists a current value in both these counterpoise system. Whereas, the helical coil has zero current, because one of the terminals of the secondary side of the counterpoise is freely suspended in the air. Thus, forming an open circuit voltage.

6.2 Multiple Receiver Capability

Power was transmitted along a 8 m metal sheet, the receivers were placed in various arbitrary configurations. The power reception was uniform despite of the configuration. However, beyond 8 m, a marginal degradation in power reception of the farthest receiver with respect to transmitter was observed. The table ST 6 lists the power transfer metrics for

Table ST 4 – Power transfer metrics for 20 Watt Halogen load across 2.7 $meters$: DC RMS Voltages and Currents

Receiver counterpoise type	Receiver	Transmitter
Helical coil ($\lambda/2$)	11.64 V, 0.92 A	20.2 V, 1.03 A
Wire ($\lambda/4$)	12V, 0.796 A	20.21V, 1.03 A
Metal plate-Wire	11.54 V, 0.69A	21.95V, 1.03 A

Table ST 5 – RMS Current and Voltage Buildup Across The Counterpoise

Counterpoise type	Voltage	Current	Remarks
Helical coil	318.6 V	0 A	Air suspended open terminals
Wire ($\lambda/4$)	43.82V	0.361.1 A	Placed on the earth ground
Metal plate-Wire	32.8 V	0.23A	Placed on the earth ground

multiple receivers. Both the receivers show approximately the same power reception capabilities. However, as compared to single transmitter- receiver power transfer efficiency, the 1 transmitter to 2 receiver efficiency sees an increment from 51.4 $\%$ to 66 $\%$.

Table ST 6 – Two receiver power transfer and loss ($watts$) across 8 $meters$ of metal sheet

Transmitted	Rx1	Rx2	Loss
40	13.15	13.25	13.6

Table ST 7 – Two receiver power transfer and loss ($watts$) across 15 $meters$ of metal sheet

Transmitted	Rx1	Rx2	Loss
40	4.78	4.05	31.17

The table ST 7 shows the multi receiver capability at 15 m, the overall efficiency is 22%. Beyond this range, the power transfer drops below 10%. With proper optimization of thickness of coils and spacing, one can obtain higher values of power transfer range.

6.3 Effect on other devices in vicinity

In the previous sections it has been pointed out that, other devices in vicinity have to be of electrically comparable lengths, apart from being resonant. A Samsung Galaxy Note 5 mobile phone was used as a test device (with an inbuilt wireless charging receiver unit, tuned at 13.3MHz). The mobile phone was kept on the metal sheet, 25 $Watts$ of power was fed into the transmitter side at 13.3MHz and 27 MHz. The wireless receiver unit of the phone was unable to pick the power. It was found that the phone's functioning was normal, with normal touch screen response times and internet access. See the video in the supporting information. Two more test subjects were chosen, which included a table lamp with an LED bulb and a 13 $inch$ laptop (laptop was kept in ON status). Both the test devices were subjected to 50 $watts$ of transmitter power. None of the test devices showed any abnormal behavior.

6.4 Effect of metal enclosure

The table ST 8 summarizes the power transfer metrics comparison between open air and the box type partial enclosure power transfer metrics of the proposed system. The open air multi receiver efficiency is around 66 % at 8 m , while the enclosed case efficiency is 64.5 % for the same distance. The metal enclosure experimental result, clearly indicates that

Table ST 8 – Partial metal shielded power transfer metrics to two receivers. Transmitted power 40 $watts$ along 8 m metal

	Rx1	Rx2
Open	13.15	13.25
Partial Box Enclosure	13.12	12.68

the helical coil counterpoise plays no role in the power transmission through radiation. As claimed earlier, the helical coil counterpoise drives the receiver terminals to a high voltage. Therefore, the proposed system is non-radiative[S15–S19].

Fig. S 15 – Shields deployed at receiving units 1 and 2.

7 Power Demo

https://youtu.be/UOc42vG9Vhs

8 Metal Neutral

https://youtu.be/6dqdgtNcEQI

9 Electronic devices in vicinity

https://youtu.be/7UPf7M1EiiE

10 Multi Receiver

https://youtu.be/qRQKoeCV-8k

11 Tx in The Metal Enclosure

https://youtu.be/t-_HAqxcnkI

References

[S1] Balanis, C.A. Antenna Theory: Analysis and Design (John Wiley & Sons, NY, 2005).

[S2] Best, S. R. Optimizing the Receiving Properties of Electrically Small HF Antennas. *URSI Radio Science Bulletin* **2016**, 13(2016).

[S3] Ziolkowski, R. W. Efficient Electrically Small Antenna Facilitated by a NearField Resonant Parasitic. *IEEE Antennas and Wireless Propagation Letters* **7**, 581-584(2008).

[S4] Malik, J., Oruganti, S. K., Song, S., Ko, N. Y., & Bien, F. Electromagnetically induced transparency in sinusoidal modulated ring resonator. *Appl. Phys. Lett.* **112**, 234102(2018).

[S5] Van Neste, C.W., Hull, R., Hawk, J.E., Phani A., & Thundat, T. Electrical excitation of the local earth for resonant, wireless energy transfer. *Cambridge Wireless Power Journal*, **3**, 117-125(2016).

[S6] Van Neste, C.W., Hawk, J.E., Phani, A., Backs, J.A.J, Hull, R., Abraham, T., Glassford, S.J., Pickering, A.K., & Thundat,T. Single-contact transmission for the quasi-wireless delivery of power over large surfaces. *Cambridge Wireless Power Journal* **1**, 75-82(2014).

[S7] Schelkunoff, S. Anatomy of Surface waves. *IRE Trans. on Antenna and Propagation* **7**, 133-139 (1959).

[S8] Sarkar,T. K., Abdallah, M. N., Salazar-Palma, M., & Dyab, W. M. Surface Plasmons-Polaritons, Surface Waves, and Zenneck Waves: Clarification of the terms and a description of the concepts and their evolution. *IEEE Antennas and Propagation Magazine* **59**, 77-93(2017).

[S9] Sarkar,T.K., Dyab,W.M., Abdallah, M.N.,Salazar-Palma, M., Prasad, M.V.S.N., & Ting, S. Application of the Schelkunoff formulation to the Sommerfeld problem of a vertical electric dipole radiating over an imperfect ground. *IEEE Trans. on Antennas and Propagation* **62**, 4162-4170 (2014).

[S10] Barlow, H.M. & Cullen, A.L. Surface Waves. *Proceed. of the IEE - Part III: Radio and Comm. Engineering* **100**, 329-341 (1953).

[S11] Kurs, A., Karalis, A., Moffatt, R., Joannopoulos, J. D., Fisher, P., & Soljacic, M. Wireless Power Transfer via Strongly Coupled Magnetic Resonances. *Science* **317**, 83-86 (2007).

[S12] Li, J., Huang, X., Chen, C., Tan, L., Wang W. & Guo,J. Effect of metal shielding on a wireless power transfer system. *AIP Advances* **7**, 056675 (2017).

[S13] Jangal,F., Bourey, N., Darces, M., Issac, F. & Hélier, M. Observation of Zenneck-Like Waves over a Metasurface Designed for Launching HF Radar Surface Wave. *Hindawi, International J. of Antennas and Propagation* **2016**,1 (2016).

[S14] Sommerfeld, A. N. Über die Ausbreitung der Wellen in der drahtlosen Telegraphie *Ann. d. Phys.* **28**, 665-736(1909).

[S15] Oruganti, S.K., & Bien F. Investigation of near-field wireless energy transfer for through metal-wall applications. *IEEE Wireless Power Transfer Conference (WPTC)*, 247(2014).

[S16] Oruganti, S.K., Heo, S.H., Ma, H., & Bien, F. Wireless energy transfer based transceiver systems for power and/or high-data rate transmission through thick metal walls using sheet-like wave-guides. *Electron. Lett.* **50**, 886(2014).

[S17] Oruganti, S. K., Kaiyrakhmet, O. & Bien, F. Wireless power and data transfer system for internet of things over metal walls and metal shielded environments. *URSI Asia-Pacific Radio Science Conference*, 318(2016).

[S18] Oruganti, S.K., Heo, S.H., Ma, H., & Bien, F. Wireless energy transfer: touch/proximity/hover sensing for large, contoured displays and industrial applications. *IEEE Sensors Journal* **15**, 2062(2015).

[S19] Oruganti,S.K., Thesis, *Ulsan National Institute of Science and Technology*, 2016.

[S20] Ahlbom, A., et al. Guidelines For Limiting Exposure To Time-Varying Electric, Magnetic, and Electromagnetic Fields (up to 300 GHz). *Health Phys.* **74**, 494(1998)